

# Exploring the Relationship between Composition and Li-Ion Conductivity in the Amorphous Li–La–Zr–O System

Dexin Zhang, Yiwei You, Fulun Wu, Xinrui Cao, Tie-Yu Lü, Yang Sun, Zi-Zhong Zhu, and Shunqing Wu\*



Cite This: ACS Materials Lett. 2024, 6, 1849–1855



Read Online

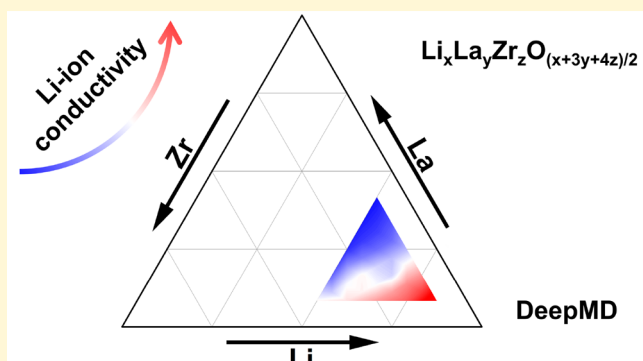
ACCESS |

Metrics & More

Article Recommendations

Supporting Information

**ABSTRACT:** Amorphous Li–La–Zr–O (a-LLZO), a promising candidate for solid electrolytes in all-solid-state Li batteries, demonstrates exceptional dendrite-inhibiting properties. By adjustment of its elemental composition, the Li-ion conductivity of a-LLZO can be modulated. In this study, we developed an interatomic potential function based on machine learning to describe amorphous LLZO systems with varying compositions. The relationship between element ratios and Li-ion conductivity is investigated by utilizing molecular dynamics simulations covering a wide range of spatial and temporal scales. Our results indicate that the degree of aggregation between La–La atoms is more severe than that between Zr–Zr atoms. Maintaining a constant Li content while increasing the level of Zr and reducing the level of La in the amorphous structure can create additional vacancies and promote Li ion diffusion.



With the rapid development of portable electronic devices and electric vehicles, there are increasing demands for higher energy density and safety in Li-ion batteries. The use of Li metal as an anode can significantly enhance the energy density of the battery.<sup>1,2</sup> However, traditional lithium-ion batteries using liquid electrolytes cannot effectively prevent the formation of lithium dendrites, posing safety risks.<sup>3</sup> To address this issue, researchers have shifted their focus to solid-state electrolytes. Among the various solid-state electrolyte materials, garnet  $\text{Li}_7\text{La}_3\text{Zr}_2\text{O}_{12}$  (LLZO) has garnered attention due to its exceptional thermal stability, high room-temperature  $\text{Li}^+$  conductivity, and wide electrochemical window.<sup>4–7</sup> However, in practical production, challenges arise from Li dendrite growth along the interface<sup>8</sup> and high interfacial impedance,<sup>9</sup> hindering the application of LLZO. To address these issues, Kim et al.<sup>10</sup> employed Al doping to promote grain growth and reduce the number of grain boundaries. Chen et al.<sup>11</sup> even achieved a Li-ion conductivity at the grain boundaries three times higher than that of the bulk phase through Al doping. In addition to mitigating the obstruction of lithium ions by grain boundaries, preparing amorphous Li–La–Zr–O films without grain boundaries is also an effective approach. Kalita et al.<sup>12</sup> successfully prepared smooth, dense, and uniform a-LLZO films using radio

frequency magnetron sputtering, demonstrating a  $\text{Li}^+$  conductivity of  $4 \times 10^{-7} \text{ S cm}^{-1}$ . The amorphous Li–La–Zr–O films prepared by Sastre et al.<sup>13</sup> showed promising potential in maintaining high current densities without causing short circuits due to Li dendrite infiltration. To further enhance the Li-ion conductivity of amorphous LLZO, researchers have introduced additional Li elements during the preparation process. Bui et al.<sup>14</sup> successfully synthesized Li-rich amorphous Li–La–Zr–O (a-LLZO) electrolytes using the sol–gel method, resulting in an ionic conductivity range of  $3.0 \times 10^{-8} \text{ S cm}^{-1}$  ( $\text{Li}_8\text{La}_2\text{Zr}_2\text{O}_{11}$ ) to  $1.18 \times 10^{-6} \text{ S cm}^{-1}$  ( $\text{Li}_{18}\text{La}_2\text{Zr}_2\text{O}_{16}$ ).

Our previous study has demonstrated the influence of elemental composition changes on Li-ion conductivity in amorphous LLZO systems. However, conducting a comprehensive study of elemental variations in LLZO using *Ab Initio*

Received: December 9, 2023

Revised: March 30, 2024

Accepted: April 1, 2024

Published: April 5, 2024



ACS Publications

© 2024 American Chemical Society

1849

<https://doi.org/10.1021/acsmaterialslett.3c01558>  
ACS Materials Lett. 2024, 6, 1849–1855

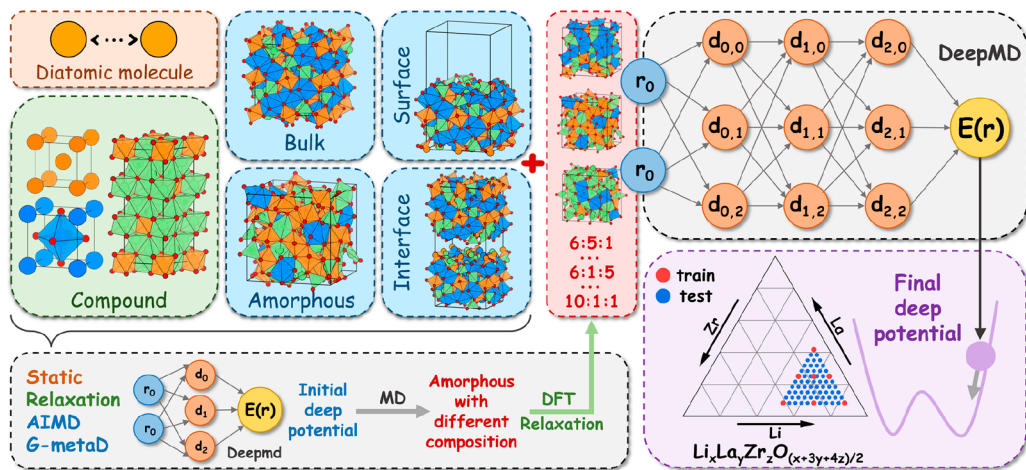


**Figure 1.** Flowchart of the interatomic potential training set and its iterations.

Molecular Dynamics (AIMD) simulations are computationally expensive. To overcome this challenge, interatomic potential functions can be trained by using deep neural networks (DNNs) based on density functional theory (DFT) data, offering computational efficiency. The potential of machine learning in condensed matter research was initially proposed by Behler and Parrinello.<sup>15</sup> Over time, various interatomic potentials have been developed, including Gaussian approximation potential (GAP),<sup>16</sup> moment tensor potential (MTP), gradient domain machine learning (GDML),<sup>17</sup> and Deep Potential Molecular Dynamics (DPMD).<sup>18</sup> Among these methods, the DeePMKit<sup>19</sup> package employs DNNs to train interatomic potential functions using *ab initio* data, such as total potential energy, atomic force, and virial functions, for a range of atomic configurations. These DNN-based interatomic potentials accurately reproduce the potentials and forces within the training data set, proving effective for molecular dynamics simulations.<sup>20–23</sup> To construct an interatomic potential function that adequately describes LLZO systems with diverse element ratios, the careful selection of the training set is essential.

In this work, we developed an interatomic potential function capable of accurately describing amorphous LLZO systems with various element ratios. To achieve this, we employed a pretraining method and iteratively incorporated new training sets. Using this potential function, we conducted calculations to investigate the relationship between different element ratios and Li-ion conductivity. Additionally, we analyzed the influence of individual elements on the Li-ion conductivity.

Our first-principles calculations were conducted using the Vienna *Ab initio* Simulation Package (VASP).<sup>24,25</sup> The projected augmented wave (PAW)<sup>26</sup> method was employed for the calculations. The electron exchange-correlation function was treated within a spin-polarized generalized gradient approximation (GGA) parametrized by Perdew–Burke–Ernzerhof (PBE).<sup>27</sup> The chosen cutoff energy was 500 eV. The k-point grid is automatically generated with KSPACING = 0.2 Å<sup>-1</sup> (VASP input tag).

During the training process of the deep potential (DP) model using the DeePMKit<sup>18</sup> package, a smoothing method is employed. In this study, the model considers a cutoff radius of 6.0 Å to account for neighboring atoms, and the inverse distance is gradually adjusted between the range of 0.5 to 6 Å to ensure a smooth transition. The neural network architecture

comprises a filtering network with three hidden layers [10, 20, 40] and a fitting network with [120, 120, 120] layers. Random parameters are initialized for the neural network, and the model undergoes 7,000,000 training steps. The training is performed using the Adam stochastic gradient descent method,<sup>28</sup> which results in an exponential decrease in the learning rate starting from 0.001. The decay step is set at 2000, and the decay rate is set at 0.996.

The loss function  $L$  was defined as follows

$$L(p_e, p_f, p_\xi) = \frac{p_e}{N} \Delta E^2 + \frac{p_f}{3N} \sum_i |\Delta F_i|^2 + \frac{p_\xi}{9N} \|\Delta \Xi\|^2 \quad (1)$$

where  $\Delta E$ ,  $\Delta F_i$ , and  $\Delta \Xi$  represent the mean square errors in energy, force, and virial, respectively. The prefactors for energy, force, and virial were adjusted throughout the training. Initially, the energy prefactor ( $p_e$ ) and virial prefactor ( $p_\xi$ ) started at a value of 0.02 and gradually increased until it reached 1. Similarly, the force prefactor ( $p_f$ ) started at 1000 and linearly decreased to a final value of 1.

To construct the interatomic potential and develop a deep learning model capable of accurately describing LLZO systems, with varying element ratios, a training set and a training process were employed, as illustrated in Figure 1.

The initial training set for the interatomic potential comprises three components:

1. Diatomic Molecular Systems: This component involves diatomic molecular systems with varying atomic distances ranging from 1 to 4 Å. Static calculations are performed to obtain the necessary data.
2. Simple Substances and Compounds: Simple substances, consisting of Li, La, Zr, and O elements, as well as binary and ternary compounds, are downloaded from Materials Project.<sup>29</sup> The lattice scale was scaled within the range of 0.8 to 1.2, and subsequent atomic relaxation calculations were performed to generate the necessary data.
3. LLZO Structure Models at Different Temperatures: This component encompasses LLZO models at different temperatures, including tetragonal phase, cubic phase, amorphous phase, and surface interface models. These structures are derived through AIMD simulations, followed by atomic relaxation calculations, to generate the required data. However, it is important to note that

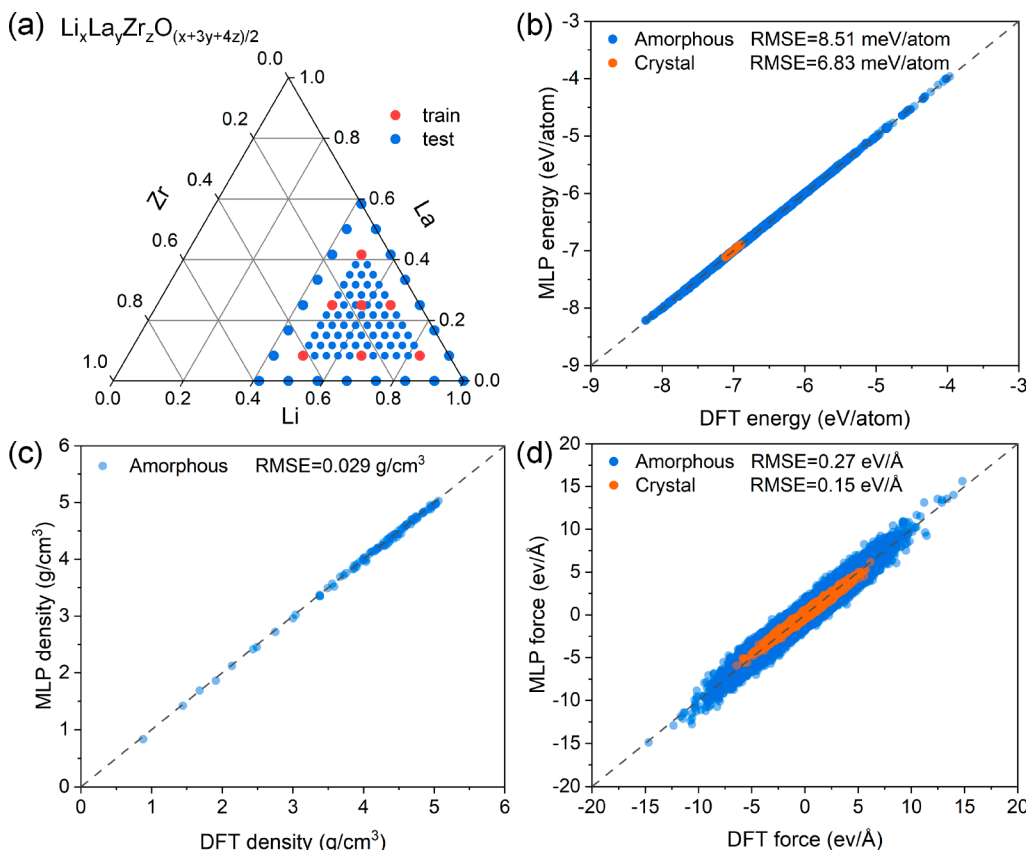


**Figure 2.** (a) Schematic diagram of the proportion of training set and test set elements. (b–d) DP vs DFT energies, forces, and densities for the Li–La–Zr–O system in the validation data.

AIMD simulations have limitations in sampling configurations near high energy barriers. In this work, to overcome this limitation, we adopted the metadynamics method based on the abstract atomic environment space (G-metaD) proposed by Yoo et al.<sup>30</sup> This method introduces a bias potential to enhance sampling and explore configurations that may deviate from the Boltzmann distribution.

The model undergoes 4,000,000 training steps using the initial training set to obtain the first-generation potential function. Subsequently, molecular dynamics (MD) simulations of amorphous LLZO are performed using first-generation potential functions to obtain structural models for the different components. To generate a new training set, atomic relaxation calculations are conducted using DFT. The old and new training sets are then merged, and the model is retrained for 7,000,000 steps to obtain the final potential function. In Figure 1, located in the lower right corner, the phase diagram displays the proportion of elements represented in red, which corresponds to the training set. Conversely, the proportion of elements within the blue region is used for testing. This testing allowed us to evaluate the generalization ability of the interatomic potential function. Principal Component Analysis (PCA)<sup>31</sup> was employed to extract the key features of the local atomic environment. As depicted in Figure S1, through iterative processes, the coverage between the test set and the training set improved from 88% to 97%. This outcome indicates that our sampling of the local atomic environment has been comprehensive enough to ensure the accuracy of the crystal structure prediction (CSP).

To assess the accuracy of the DNN interatomic potentials, we conducted a comparison of energies and forces predicted by the DP model with those obtained from DFT. As illustrated in Figure 2(b–d), the DP model demonstrated high accuracy in predicting the energy, force, and density of both crystalline and amorphous LLZO, in comparison to the DFT results. The test results reveal a strong correlation between the DP predictions and the DFT outcomes. The root-mean-square error (RMSE) for force is less than 0.27 eV/Å, while the RMSE for energy is less than 8.51 meV/atom.

To validate the accuracy of the DP model in describing the local structures of both crystalline and amorphous phases, we conducted tests on the radial distribution function (RDF) for cubic LLZO and amorphous Li–La–Zr–O. Figure S2 illustrates the excellent agreement between the AIMD and DPMD simulations for the radial distribution function  $g(r)$ .

To ensure that the DP model can accurately describe the trend of Li-ion conductivity as a function of element ratios, we utilized the model to prepare amorphous LLZO structures with various element ratios using a melt-quenching molecular dynamics method.<sup>32</sup> Throughout the process, we carefully balanced the number of oxygen atoms based on charge considerations, resulting in a total of over 4000 atoms. With an initial element ratio of  $\text{Li/La/Zr} = 7:3:2$ , kinetic simulations were performed at different temperatures to determine the Li-ion conductivity at room temperature, as shown in Figure 3(a). By comparing the obtained results with experimental data,<sup>12,33–40</sup> we find that they fall within a reasonable order of magnitude. As can be seen from Figure 3(b), the Li-ion conductivity of the lithium-rich amorphous LLZO prepared by

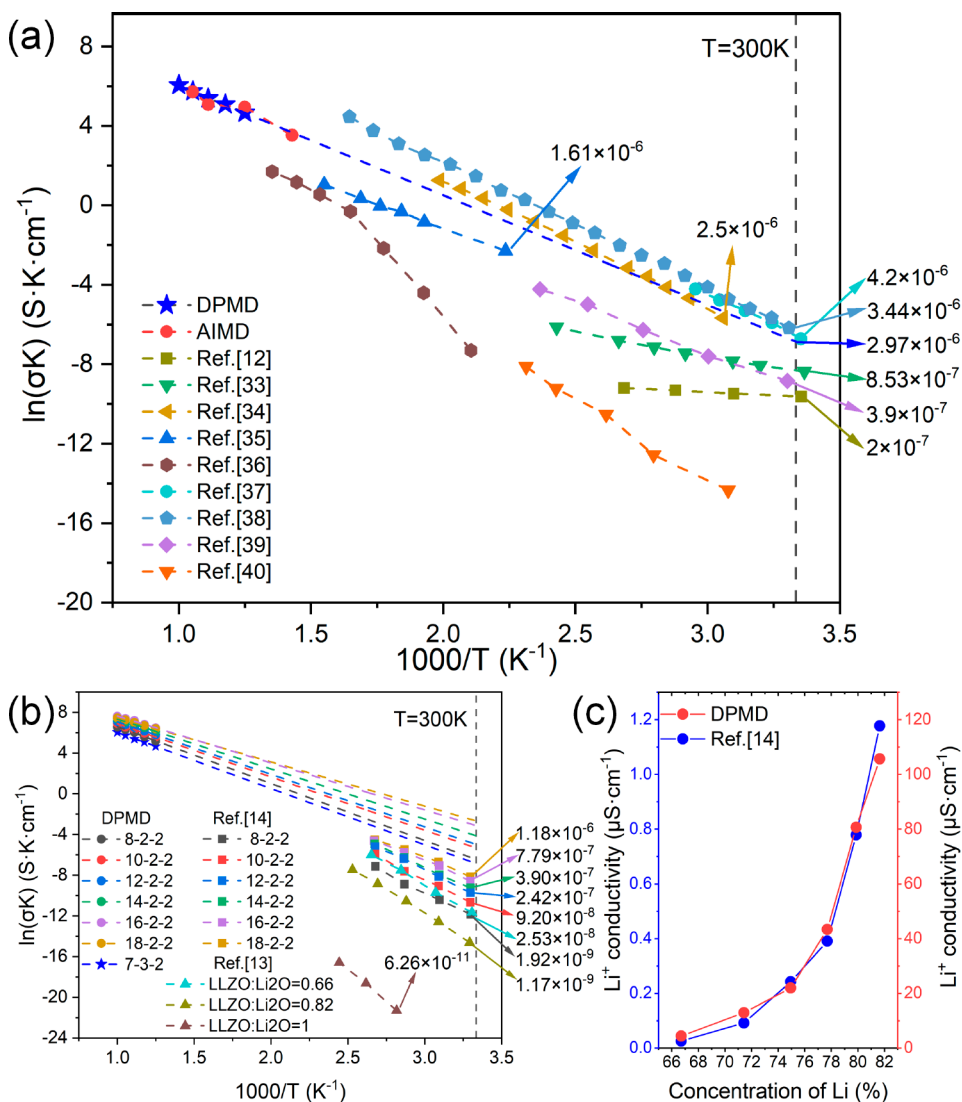


**Figure 3.** Li-ion conductivity of amorphous LLZO obtained through DPMC is compared with the experimental data. The value pointed by the arrow is the Li-ion conductivity at room temperature, in S cm $^{-1}$ . (a) The results of 7:3:2 amorphous DPMC simulations are compared with AIMD and experimental data. (b) The results of 8:2:2 to 18:2:2 amorphous DPMC simulations are compared with experimental data. (c) The trend of Li-ion conductivity as obtained from DPMC is compared with experimental data.

Bui<sup>14</sup> and Sastre<sup>13</sup> shows an increasing trend as the lithium content increases. However, different preparation methods resulted in large order of magnitude differences between the two groups. Furthermore, our study reveals that the Li-ion conductivity of amorphous LLZO prepared with element ratios ranging from 8:2:2 to 18:2:2 exhibits a consistent variation trend with the experimental observations,<sup>14</sup> as depicted in Figure 3(c).

Amorphous LLZO structures with varying element ratios were prepared by using the melt-quenching molecular dynamics method. MD simulations were conducted within the temperature range of 700–900 K, and the Li-ion conductivity at 300 K was obtained through fitting. The calculation method of Li-ion conductivity is detailed in the Supporting Information. These simulation results are listed in Figure 4(a). To ensure accuracy and reliability, seven independent calculations were performed for each element ratio, and the average value of Li-ion conductivity was derived.

From Figure 4(a), it is evident that the Li-ion conductivity of amorphous LLZO increases with the rise in both Li and Zr

content. We determined the Li-site volume ratio (Li-vol) to the unit cell volume by considering the minimum distance between Li and three elements: La, Zr, and O. The calculation methodology is detailed in Figure S3. To execute this process, all Li atoms were removed from the unit cell, and spheres were generated centered on La, Zr, and O, with the radius set as the minimum distance from Li. The unoccupied space represents the potential area for the Li atoms. The results of these calculations are visually presented in Figure 4(b). It can be seen from Figure 4(c) that when the Li content remains unchanged, the Li<sup>+</sup> conductivity increases with Li-vol.

In amorphous LLZO, the structure consists of La–O and Zr–O polyhedra, creating the framework through which Li ions migrate in the voids. The aggregation of La and Zr influences Li-vol. To compare the differences in La and Zr aggregation, we generated amorphous structures with element ratios of 6:3:3 and 8:2:2 to maintain consistent La and Zr contents. Subsequently, we calculated the number of neighboring La atoms around each La atom and the number of neighboring Zr atoms around each Zr atom. The number of

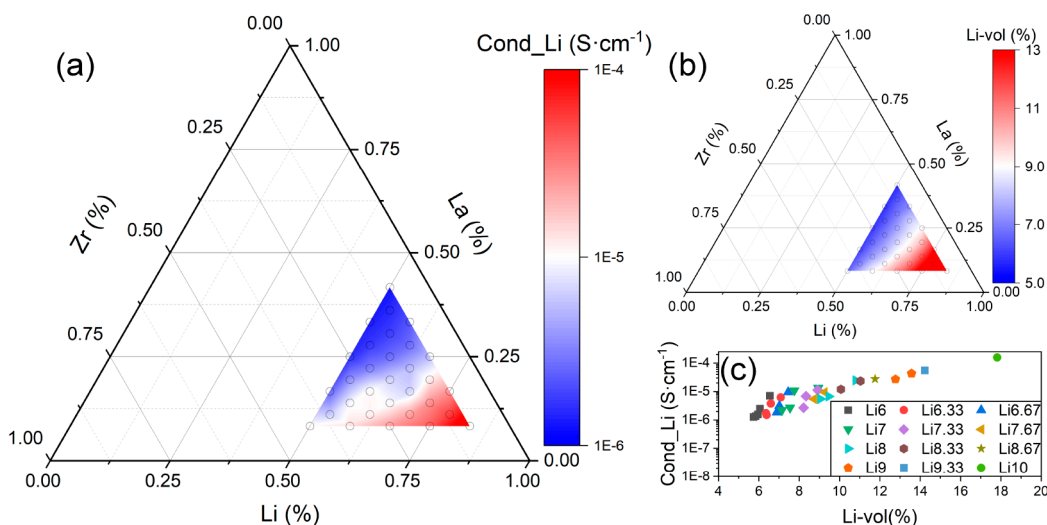


**Figure 4.** (a) Li-ion conductivity of amorphous materials with different element ratios. (b) Li-vol with different element ratios. (c) Relationship between Li-ion conductivity and Li-vol.

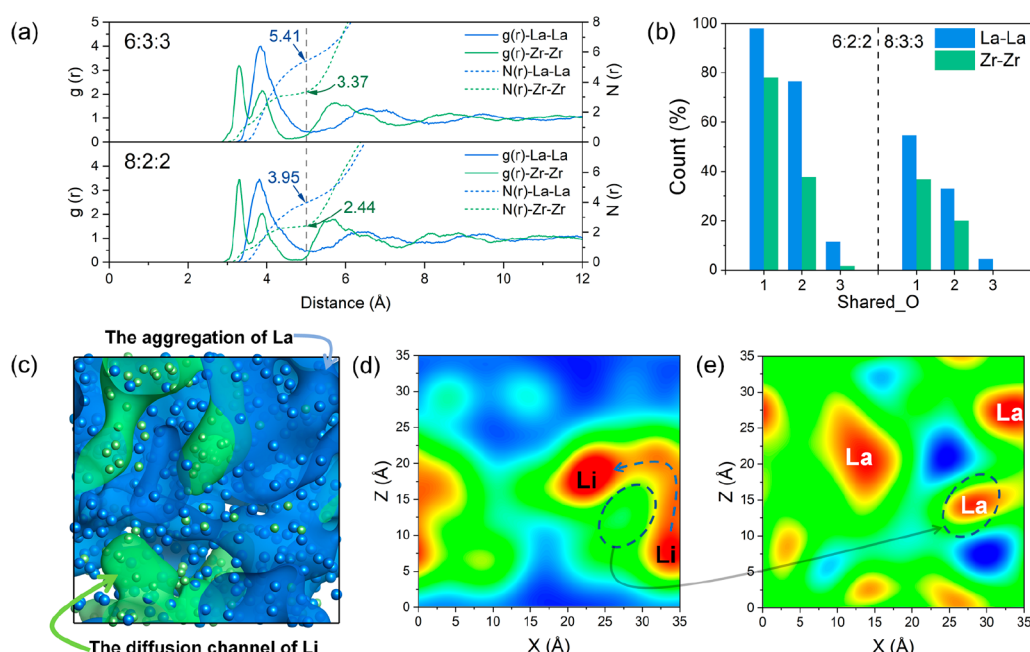


**Figure 5.** (a) Distribution of La-La and Zr-Zr in amorphous structures at 300 K.  $g(r)$  represents the probability of finding other atoms at the radius  $r$  of the central atom, and  $N(r)$  represents the number of other atoms in the sphere within radius  $r$ . (b) Number of shared  $O_2^-$  at 300 K for 6:2:2 and 8:3:3 samples. (c) The relationship between the Li migration path and La aggregation, where the blue area represents the aggregation of La atoms and the green area represents the Li migration path. (d) Density distribution of Li. (e) Density distribution of La.

other atoms around the central atom was calculated using the following formula.<sup>41</sup>

$$N(r') = 4\pi\rho \int_0^{r'} g(r)r^2 dr$$

Here,  $\rho = N/V$  is the particle number density,  $g(r)$  is the radial distribution function.  $N(r)$  represents the number of atoms in a sphere of radius  $r$ . A higher value indicates a greater aggregation of atoms. As illustrated in Figure 5(a), a cutoff distance of 5 Å was selected to assess the local aggregation scenario, revealing a tendency for La to aggregate more readily than Zr. We counted the number of shared oxygen atoms (shared\_O) within the La-O polyhedra and Zr-O polyhedra

in two samples, as shown in Figure 5(b). The results indicate that the interconnections among La-O polyhedra are closer compared to those among Zr-O polyhedra.

The aggregation of La and the tight connections between La-O polyhedra hinder the migration of Li ions. In Figure 5(c), the blue point represents the average position of La within 50 ps, while the green point depicts the superposition of the positions of Li ions that can migrate rapidly in the same time frame. This visualization reflects the impact of La aggregation on Li migration: Li ions move quickly in regions with low La aggregation. Figures 5(d) and 5(e) illustrate the distributions of Li and La on the cross-section shown in Figure 5(c), respectively. The red spectra represent regions with a

high degree of aggregation. From Figure 5(d,e), it is evident that Li ions migrate from positions with less La aggregation to other positions with lower La aggregation, bypassing areas with a high degree of La aggregation. Indeed, when analyzing Zr and La as the same element, it is observed that as the La content increases, the degree of aggregation of La and Zr in the amorphous structure also increases, as depicted in Figure S4. This increased aggregation of La and Zr inhibits the migration of Li ions, resulting in a decreased Li-ion conductivity in the system. Consequently, substituting La with Zr would create additional Li sites and enhance the likelihood of Li-ions migration.

In summary, we have successfully developed a deep neural network (DNN) interatomic potential for multicomponent Li-La-Zr-O systems using DPMD. This accomplishment establishes a valuable framework for creating interatomic potential functions applicable to complex multicomponent systems. Compared to AIMD, DPMD offers a substantial reduction in computational costs while preserving the precision of the energy and force predictions. This capability empowers us to conduct extensive molecular dynamics simulations on amorphous Li-La-Zr-O materials featuring varying elemental ratios. Furthermore, our test results confirm the congruence between the Li-ion conductivity predicted by this potential function and the experimental observations. Additionally, we calculated the dependence of the Li-ion conductivity on element ratios. Our research findings highlight that La has a higher propensity to aggregate than Zr, impeding the diffusion of Li ions. When the Li content remains constant, augmenting the Zr content and decreasing the La content can lead to an enhancement in the Li-ion conductivity.

## ■ ASSOCIATED CONTENT

### SI Supporting Information

The Supporting Information is available free of charge at <https://pubs.acs.org/doi/10.1021/acsmaterialslett.3c01558>.

Li-ion conductivity calculation, Principal Component Analysis (PCA), Radial distribution function (RDF), Schematic diagram of calculation method of Li-sites, Aggregation of La and Zr in amorphous structure ([PDF](#))

## ■ AUTHOR INFORMATION

### Corresponding Author

**Shunqing Wu** – Department of Physics, OSED, Key Laboratory of Low Dimensional Condensed Matter Physics (Department of Education of Fujian Province), Xiamen University, Xiamen 361005, China; [orcid.org/0000-0002-2545-0054](#); Email: [wsq@xmu.edu.cn](mailto:wsq@xmu.edu.cn)

### Authors

**Dexin Zhang** – Department of Physics, OSED, Key Laboratory of Low Dimensional Condensed Matter Physics (Department of Education of Fujian Province), Xiamen University, Xiamen 361005, China

**Yiwei You** – Department of Physics, OSED, Key Laboratory of Low Dimensional Condensed Matter Physics (Department of Education of Fujian Province), Xiamen University, Xiamen 361005, China; [orcid.org/0000-0003-0022-4613](#)

**Fulun Wu** – Department of Physics, OSED, Key Laboratory of Low Dimensional Condensed Matter Physics (Department of Education of Fujian Province), Xiamen University, Xiamen 361005, China

**Xinrui Cao** – Department of Physics, OSED, Key Laboratory of Low Dimensional Condensed Matter Physics (Department of Education of Fujian Province) and Fujian Provincial Key Laboratory of Theoretical and Computational Chemistry, Xiamen University, Xiamen 361005, China; [orcid.org/0000-0002-2998-8863](#)

**Tie-Yu Lü** – Department of Physics, OSED, Key Laboratory of Low Dimensional Condensed Matter Physics (Department of Education of Fujian Province), Xiamen University, Xiamen 361005, China; [orcid.org/0000-0002-9402-370X](#)

**Yang Sun** – Department of Physics, OSED, Key Laboratory of Low Dimensional Condensed Matter Physics (Department of Education of Fujian Province), Xiamen University, Xiamen 361005, China

**Zi-Zhong Zhu** – Department of Physics, OSED, Key Laboratory of Low Dimensional Condensed Matter Physics (Department of Education of Fujian Province) and Fujian Provincial Key Laboratory of Theoretical and Computational Chemistry, Xiamen University, Xiamen 361005, China; [orcid.org/0000-0001-5353-4418](#)

Complete contact information is available at:  
<https://pubs.acs.org/10.1021/acsmaterialslett.3c01558>

### Author Contributions

CRedit: Dexin Zhang data curation, investigation, methodology, validation, visualization, writing-original draft, writing-review & editing; Yiwei You investigation, methodology, validation, writing-review & editing; Fulun Wu investigation, methodology; Xinrui Cao supervision, writing-review & editing; Tie-Yu Lu supervision, writing-review & editing; Yang Sun supervision, writing-review & editing; Zi-Zhong Zhu resources, supervision; Shunqing Wu conceptualization, investigation, methodology, resources, supervision, writing-review & editing.

### Notes

The authors declare no competing financial interest.

## ■ ACKNOWLEDGMENTS

This work is supported by the National Natural Science Foundation of China (Grant No. 11874307). Shaorong Fang and Tianfu Wu from Information and Network Center of Xiamen University are acknowledged for the help with the Graphics Processing Unit (GPU) computing.

## ■ REFERENCES

- (1) Yang, L.; Cheng, X.; Gao, Y.; Ma, Y.; Zuo, P.; Du, C.; Cui, Y.; Guan, T.; Lou, S.; Wang, F.; Fei, W.; Yin, G. Lithium Deposition on Graphite Anode during Long-Term Cycles and the Effect on Capacity Loss. *RSC Adv.* **2014**, *4*, 26335–26341.
- (2) Wang, P.; Qu, W.; Song, W.; Chen, H.; Chen, R.; Fang, D. Electro-Chemo-Mechanical Issues at the Interfaces in Solid-State Lithium Metal Batteries. *Adv. Funct. Mater.* **2019**, *29*, No. 1900950.
- (3) Chen, R.; Li, Q.; Yu, X.; Chen, L.; Li, H. Approaching Practically Accessible Solid-State Batteries: Stability Issues Related to Solid Electrolytes and Interfaces. *Chem. Rev.* **2020**, *120*, 6820–6877.
- (4) Thangadurai, V.; Weppner, W.  $\text{Li}_6\text{Al}_2\text{Ta}_2\text{O}_{12}$  (A = Sr, Ba): Novel Garnet-Like Oxides for Fast Lithium Ion Conduction. *Adv. Funct. Mater.* **2005**, *15*, 107–112.
- (5) Liu, Q.; Geng, Z.; Han, C.; Fu, Y.; Li, S.; He, Y.; Kang, F.; Li, B. Challenges and Perspectives of Garnet Solid Electrolytes for All Solid-State Lithium Batteries. *J. Power Sources* **2018**, *389*, 120–134.
- (6) Ramakumar, S.; Deviannapoorani, C.; Dhivya, L.; Shankar, L. S.; Murugan, R. Lithium Garnets: Synthesis, Structure,  $\text{Li}^+$  Conductivity,  $\text{Li}^+$  Dynamics and Applications. *Prog. Mater. Sci.* **2017**, *88*, 325–411.

- (7) Hiebl, C.; Young, D.; Wagner, R.; Wilkening, H. M. R.; Redhammer, G. J.; Rettenwander, D. Proton Bulk Diffusion in Cubic  $\text{Li}_7\text{La}_3\text{Zr}_2\text{O}_{12}$  Garnets as Probed by Single X-Ray Diffraction. *J. Phys. Chem. C* **2019**, *123*, 1094–1098.
- (8) Cheng, E. J.; Sharafi, A.; Sakamoto, J. Intergranular Li Metal Propagation through Polycrystalline  $\text{Li}_{6.25}\text{Al}_{0.25}\text{La}_3\text{Zr}_2\text{O}_{12}$  Ceramic Electrolyte. *Electrochim. Acta* **2017**, *223*, 85–91.
- (9) Li, Y.; Cao, Y.; Guo, X. Influence of Lithium Oxide Additives on Densification and Ionic Conductivity of Garnet-Type  $\text{Li}_{6.75}\text{La}_3\text{Zr}_{1.75}\text{Ta}_{0.25}\text{O}_{12}$  Solid Electrolytes. *Solid State Ionics* **2013**, *253*, 76–80.
- (10) Kim, A.; Kang, J.-H.; Song, K.; Kang, B. Simultaneously Improved Cubic Phase Stability and Li-Ion Conductivity in Garnet-Type Solid Electrolytes Enabled by Controlling the Al Occupation Sites. *ACS Appl. Mater. Interfaces* **2022**, *14*, 12331–12339.
- (11) Chen, C.; Sun, Y.; He, L.; Kotobuki, M.; Hanc, E.; Chen, Y.; Zeng, K.; Lu, L. Microstructural and Electrochemical Properties of Al- and Ga-Doped  $\text{Li}_7\text{La}_3\text{Zr}_2\text{O}_{12}$  Garnet Solid Electrolytes. *ACS Appl. Energy Mater.* **2020**, *3*, 4708–4719.
- (12) Kalita, D. J.; Lee, S. H.; Lee, K. S.; Ko, D. H.; Yoon, Y. S. Ionic Conductivity Properties of Amorphous Li-La-Zr-O Solid Electrolyte for Thin Film Batteries. *Solid State Ionics* **2012**, *229*, 14–19.
- (13) Sastre, J.; Futscher, M. H.; Pompizi, L.; Aribia, A.; Priebe, A.; Overbeck, J.; Stiefel, M.; Tiwari, A. N.; Romanyuk, Y. E. Blocking Lithium Dendrite Growth in Solid-State Batteries with an Ultrathin Amorphous Li-La-Zr-O Solid Electrolyte. *Communications Materials* **2021**, *2*, 76.
- (14) Bui, T. T.; Yun, B.; Darko, K.; Shin, S. B.; Kim, J.; Hong, J.; Lee, M.; Park, S. K.; Kim, M. Solution Processing of Lithium-Rich Amorphous Li-La-Zr-O Ion Conductor and Its Application for Cycling Durability Improvement of  $\text{LiCoO}_2$  Cathode as Coating Layer. *Adv. Mater. Interfaces* **2021**, *8*, No. 2001767.
- (15) Behler, J.; Parrinello, M. Generalized Neural-Network Representation of High-Dimensional Potential-Energy Surfaces. *Phys. Rev. Lett.* **2007**, *98*, No. 146401.
- (16) Bartók, A. P.; Payne, M. C.; Kondor, R.; Csányi, G. Gaussian Approximation Potentials: The Accuracy of Quantum Mechanics, without the Electrons. *Phys. Rev. Lett.* **2010**, *104*, No. 136403.
- (17) Chmiela, S.; Tkatchenko, A.; Sauceda, H. E.; Poltavsky, I.; Schütt, K. T.; Müller, K.-R. Machine Learning of Accurate Energy-Conserving Molecular Force Fields. *Sci. Adv.* **2017**, *3*, No. e1603015.
- (18) Zhang, L.; Han, J.; Wang, H.; Car, R.; E, W. Deep Potential Molecular Dynamics: A Scalable Model with the Accuracy of Quantum Mechanics. *Phys. Rev. Lett.* **2018**, *120*, No. 143001.
- (19) Wang, H.; Zhang, L.; Han, J.; E, W. DeePMD-Kit: A Deep Learning Package for Many-Body Potential Energy Representation and Molecular Dynamics. *Comput. Phys. Commun.* **2018**, *228*, 178–184.
- (20) Chen, W.-K.; Liu, X.-Y.; Fang, W.-H.; Dral, P. O.; Cui, G. Deep Learning for Nonadiabatic Excited-State Dynamics. *J. Phys. Chem. Lett.* **2018**, *9*, 6702–6708.
- (21) Zhang, L.; Wang, H.; Car, R.; E, W. Phase Diagram of a Deep Potential Water Model. *Phys. Rev. Lett.* **2021**, *126*, No. 236001.
- (22) Calegari Andrade, M. F.; Ko, H.-Y.; Zhang, L.; Car, R.; Selloni, A. Free Energy of Proton Transfer at the Water-TiO<sub>2</sub> Interface from *Ab Initio* Deep Potential Molecular Dynamics. *Chem. Sci.* **2020**, *11*, 2335–2341.
- (23) Tang, L.; Yang, Z. J.; Wen, T. Q.; Ho, K. M.; Kramer, M. J.; Wang, C. Z. Development of Interatomic Potential for Al-Tb Alloys Using a Deep Neural Network Learning Method. *Phys. Chem. Chem. Phys.* **2020**, *22*, 18467–18479.
- (24) Kresse, G.; Hafner, J. *Ab Initio* Molecular Dynamics for Liquid Metals. *Phys. Rev. B* **1993**, *47*, 558–561.
- (25) Kresse, G.; Furthmüller, J. Efficient Iterative Schemes for *Ab Initio* Total-Energy Calculations Using a Plane-Wave Basis Set. *Phys. Rev. B* **1996**, *54*, 11169–11186.
- (26) Blöchl, P. E. Projector Augmented-Wave Method. *Phys. Rev. B* **1994**, *50*, 17953–17979.
- (27) Perdew, J. P.; Burke, K.; Ernzerhof, M. Generalized Gradient Approximation Made Simple. *Phys. Rev. Lett.* **1996**, *77*, 3865–3868.
- (28) Kingma, D. P.; Ba, J. Adam: A Method for Stochastic Optimization. *arXiv* **2014**, DOI: 10.48550/arXiv.1412.6980.
- (29) Jain, A.; Ong, S. P.; Hautier, G.; Chen, W.; Richards, W. D.; Dacek, S.; Cholia, S.; Gunter, D.; Skinner, D.; Ceder, G.; Persson, K. A. Commentary: The Materials Project: A Materials Genome Approach to Accelerating Materials Innovation. *APL Mater.* **2013**, *1*, No. 011002.
- (30) Yoo, D.; Jung, J.; Jeong, W.; Han, S. Metadynamics Sampling in Atomic Environment Space for Collecting Training Data for Machine Learning Potentials. *npj Comput. Mater.* **2021**, *7*, 131.
- (31) Abdi, H.; Williams, L. J. Principal Component Analysis: Principal Component Analysis. *WIREs. Comput. Stat.* **2010**, *2*, 433–459.
- (32) Jarolimek, K.; De Groot, R. A.; De Wijs, G. A.; Zeman, M. First-Principles Study of Hydrogenated Amorphous Silicon. *Phys. Rev. B* **2009**, *79*, No. 155206.
- (33) Chen, R.-J.; Huang, M.; Huang, W.-Z.; Shen, Y.; Lin, Y.-H.; Nan, C.-W. Sol-Gel Derived Li-La-Zr-O Thin Films as Solid Electrolytes for Lithium-Ion Batteries. *J. Mater. Chem. A* **2014**, *2*, 13277.
- (34) Tadanaga, K.; Egawa, H.; Hayashi, A.; Tatsumisago, M.; Mosa, J.; Aparicio, M.; Duran, A. Preparation of Lithium Ion Conductive Al-Doped  $\text{Li}_7\text{La}_3\text{Zr}_2\text{O}_{12}$  Thin Films by a Sol-Gel Process. *J. Power Sources* **2015**, *273*, 844–847.
- (35) Park, J. S.; Cheng, L.; Zorba, V.; Mehta, A.; Cabana, J.; Chen, G.; Doeffer, M. M.; Richardson, T. J.; Park, J. H.; Son, J.-W.; Hong, W.-S. Effects of Crystallinity and Impurities on the Electrical Conductivity of Li-La-Zr-O Thin Films. *Thin Solid Films* **2015**, *576*, 55–60.
- (36) Rawlence, M.; Garbayo, I.; Buecheler, S.; Rupp, J. L. M. On the Chemical Stability of Post-Lithiated Garnet Al-Stabilized  $\text{Li}_7\text{La}_3\text{Zr}_2\text{O}_{12}$  Solid State Electrolyte Thin Films. *Nanoscale* **2016**, *8*, 14746–14753.
- (37) Loho, C.; Djenicadic, R.; Bruns, M.; Clemens, O.; Hahn, H. Garnet-Type  $\text{Li}_7\text{La}_3\text{Zr}_2\text{O}_{12}$  Solid Electrolyte Thin Films Grown by CO<sub>2</sub>-Laser Assisted CVD for All-Solid-State Batteries. *J. Electrochem. Soc.* **2017**, *164*, A6131–A6139.
- (38) Sastre, J.; Priebe, A.; Döbeli, M.; Michler, J.; Tiwari, A. N.; Romanyuk, Y. E. Lithium Garnet  $\text{Li}_7\text{La}_3\text{Zr}_2\text{O}_{12}$  Electrolyte for All-Solid-State Batteries: Closing the Gap between Bulk and Thin Film Li-Ion Conductivities. *Adv. Mater. Interfaces* **2020**, *7*, No. 2000425.
- (39) Song, S.; Xu, Y.; Ruan, Y.; Wang, H.; Zhang, D.; Thokchom, J.; Mei, D. Isomeric Li-La-Zr-O Amorphous–Crystalline Composite Thin-Film Electrolytes for All-Solid-State Lithium Batteries. *ACS Appl. Energy Mater.* **2021**, *4*, 8517–8528.
- (40) Koresh, I.; Klein, B. A.; Tang, Z.; Michaelis, V. K.; Troczynski, T. Li Ion Transport Properties of Amorphous/Crystalline Li-La-Zr-Nb-O Solid Electrolyte Thick Films Prepared by Suspension Plasma Spraying. *Solid State Ionics* **2022**, *380*, No. 115938.
- (41) Cristiglio, V.; Cuello, G. J.; Piarristeguy, A. A.; Pradel, A. The Coordination Number Calculation from Total Structure Factor Measurements. *J. Non-Cryst. Solids* **2009**, *355*, 1811–1814.